

ARTICLE

OPEN

Direct observation of ferroelectricity in two-dimensional MoS₂

Alexey Lipatov^{1,8}, Pradeep Chaudhary^{2,8}, Zhao Guan^{3,8}, Haidong Lu², Gang Li¹, Olivier Crégut⁴, Kokou Dodzi Dorkenoo⁴, Roger Proksch⁵, Salia Cherifi-Hertel⁴, Ding-Fu Shao¹, Evgeny Y. Tsymbal¹, Jorge Íñiguez^{1,6,7,✉}, Alexander Sinitskii^{1,✉} and Alexei Gruverman¹

Recent theoretical predictions of ferroelectricity in two-dimensional (2D) van der Waals materials reveal exciting possibilities for their use in scalable low-power electronic devices with polarization-dependent functionalities. These prospects have been further invigorated by the experimental evidence of the polarization response in some transition metal chalcogenides (TMCs)—a group of narrow-band semiconductors and semimetals with a wealth of application potential. Among the TMCs, molybdenum disulfide (MoS₂) is known as one of the most promising and robust 2D electronic materials. However, in spite of theoretical predictions, no ferroelectricity has been experimentally detected in MoS₂, while the emergence of this property could enhance its potential for electronics applications. Here, we report the experimental observation of a stable room-temperature out-of-plane polarization ordering in 2D MoS₂ layers, where polarization switching is realized by mechanical pressure induced by a tip of a scanning probe microscope. Using this approach, we create the bi-domain polarization states, which exhibit different piezoelectric activity, second harmonic generation, surface potential, and conductivity. Ferroelectric MoS₂ belongs to the distorted trigonal structural 1T' phase, where a spontaneous polarization is inferred by its *P3m1* space-group symmetry and corroborated by theoretical modeling. Experiments on the flipped flakes reveal that the 1T'-MoS₂ samples consist of the monolayers with randomly alternating polarization orientation, which form stable but switchable “antipolar” head-to-head or tail-to-tail dipole configurations. Mechanically written domains are remarkably stable facilitating the application of 1T'-MoS₂ in flexible memory and electromechanical devices.

npj 2D Materials and Applications (2022)6:18; https://doi.org/10.1038/s41699-022-00298-5

INTRODUCTION

The emergence of ferroelectricity in two-dimensional (2D) materials is ascribed to the loss of a center of symmetry in the intrinsically centrosymmetric structures. Indeed, in the structures of naturally occurred 2D transition metal chalcogenides (TMCs), the projections of their atomic positions on the out-of-plane axis are usually centrosymmetric¹. Several mechanisms have been proposed to explain the possibility of a stable polar state in these materials. One is related to the polar distortions in symmetric monolayers. It was predicted that the in-plane trimerization in monolayer 1T-MoS₂ could break the inversion symmetry and introduce the out-of-plane polarization². In addition, stacking of structurally symmetric nonpolar monolayers can break the inversion symmetry and introduce ferroelectricity in the bulk structure as was observed experimentally for T_d-WTe₂³. Another mechanism is related to the intrinsic polar symmetry, such as in In₂Se₃, where the ferroelectricity was predicted to arise due to the vertical displacement of Se atoms⁴. Chemical functionalization can also transform 2D materials into a ferroelectric state as predicted for functionalized phosphorene⁵ and graphanol⁶.

In contrast to the wealth of theoretical work predicting ferroelectricity in 2D materials, experimental confirmation of these predictions is lagging due to the generally small values of polarization and increased leakage, which makes any dielectric and ferroelectric measurements challenging⁷. Several notable examples of experimental observation include the out-of-plane polarization in multilayered α-In₂Se₃ revealed by a combination of

structural, optical and electrical characterization^{8,9}, polarization-dependent bi-stable conductance in two- and three-layer WTe₂³, robust in-plane polarization in SnTe and SnS^{10,11}, domain structure in WTe₂ single crystals¹² and in CulnP₂S₆ flakes¹³, and switchable in-plane polarization in thin flakes of hybrid perovskites¹⁴.

So far, however, no ferroelectricity has been observed experimentally in 2D molybdenum disulfide MoS₂, a well-studied TMC material with a set of technologically appealing properties suitable for application in flexible electronics, transparent transistor devices, and the related fields of biological and chemical technologies^{15–20}. Experimental realization of a ferroelectric state in MoS₂, which was predicted theoretically², could reveal a new physics of this material and significantly broaden the range of its potential applications. The easily changeable intralayer stacking structure of the S-Mo-S layers in MoS₂ gives rise to a variety of 2D MoS₂ polymorphs, which include semiconducting 2H²⁰ and semi-metallic 1T²¹ phases. The most thermodynamically stable 2H phase has a layered structure, in which Mo atoms are surrounded by six S atoms in trigonal prismatic coordination (see Supplementary Fig. 1). In centrosymmetric 1T-MoS₂, the Mo atoms are coordinated with six S atoms in an ideal octahedral arrangement. The 1T-MoS₂ phase is, however, unstable with respect to the Peierls distortion resulting in the formation of the monoclinic (distorted octahedral) 1T'-MoS₂ phase, which is characterized by Mo zigzag chains and S atoms arranging in deformed trigonal antiprisms around the Mo atoms²². Despite the structural distortions, the 1T' phase, similar to the 2H and 1T phases, is

¹Department of Chemistry, University of Nebraska, Lincoln, NE 68588, USA. ²Department of Physics and Astronomy, University of Nebraska, Lincoln, NE 68588, USA. ³Key Laboratory of Polar Materials and Devices and Department of Electronics, East China Normal University, Shanghai 200241, China. ⁴Université de Strasbourg, CNRS, Institut de Physique et Chimie des Matériaux de Strasbourg, UMR 7504, Strasbourg 67000, France. ⁵Asylum Research, an Oxford Instruments Company, Santa Barbara, CA, USA. ⁶Department of Physics and Materials Science, University of Luxembourg, 41 Rue du Brill, L-4422 Belvaux, Luxembourg. ⁷Department of Materials Research and Technology, Luxembourg Institute of Science and Technology, 5 Avenue des Hauts-Fourneaux, L-4362 Esch/Alzette, Luxembourg. ⁸These authors contributed equally: Alexey Lipatov, Pradeep Chaudhary, Zhao Guan. [✉]email: jorge.iniguez@list.lu; sinitskii@unl.edu; alexei_gruverman@unl.edu

centrosymmetric and, thus, non-polar. The earlier theoretical assertion of ferroelectricity in 1T-MoS₂² is based on the condensation of a soft phonon mode causing a phase transformation to another distorted 1T-MoS₂ phase, the non-centrosymmetric d1T phase with a tripled unit cell. The in-plane movement of the Mo atoms breaks the symmetry among the S atoms along the out-of-plane direction creating a z-oriented polar distortion. However, the predicted ferroelectric phase of MoS₂ remains elusive.

Here we discover emergent ferroelectricity in the recently reported 1T'-MoS₂ phase²³. The distorted trigonal 1T'-MoS₂ phase belongs to the space group *P3m1*, which has two topologically equivalent crystal structures related to each other by the inversion symmetry operation, designating its ferroelectric nature. Polarization reversal in the 1T'-MoS₂ phase has been realized via a voltage-free approach by using a tip of a scanning probe microscope (SPM) pressed against the sample surface. Facilitated by the flexoelectric effect, a tip-induced strain gradient generates a flexoelectric field much like an applied external voltage, but in a manner more resilient to the electronic screening and leakage, resulting in a stable bi-domain configuration with out-of-plane polarization detected by piezoresponse force microscopy (PFM). First-principles calculations confirm the presence of spontaneous polarization in 1T'-MoS₂ as well as the existence of stable head-to-head (H-H) and tail-to-tail (T-T) dipole configurations, which have been experimentally revealed by the experiments involving the flipped MoS₂ flakes.

RESULTS AND DISCUSSION

The 1T-MoS₂ samples were prepared by the lithiation of the multilayer 2H-MoS₂ nanosheets with thicknesses ranging from 5 to 20 nm deposited on conductive Pt/SiO₂/Si substrates (see "Methods" for details)^{24,25}. Observation of the color change of the lithiated flakes provides preliminary verification of the intended 2H phase conversion to the 1T phase, which has a darker color (Fig. 1a). The emergence of additional Raman peaks at 155, 225, 289, and 328 cm⁻¹ corresponding to the J₁, J₂, E_{1g}, and J₃ modes of the 1T phase (see Supplementary Fig. 2) further confirms the transition from the 2H to the 1T phase^{22,26–28}. To perform high-resolution structural characterization, the freshly exfoliated and lithiated MoS₂ flakes were transferred on a transmission electron microscopy (TEM) grid. As expected, selected area electron diffraction (SAED) patterns (acquired from the regions of several hundred nanometers in the lateral dimensions) show a significant difference between the two phases (Fig. 1b, c). While the 2H-MoS₂ flakes exhibit a hexagonal arrangement of bright reflection spots in the SAED pattern (Fig. 1b), the emergence of the superstructure spots can be seen in SAED of the lithiated MoS₂ flakes, which corresponds to the doubling of the unit cell parameters (Fig. 1c). This pattern is indicative of the formation of the 1T' phase (Fig. 1d), one of the distorted variants of 1T-MoS₂, which has $\sim 2a_0 \times 2a_0$ superstructure, where a_0 is the lattice parameter of 2H-MoS₂²⁹. The uniform appearance of the lithiated flakes in TEM (Fig. 1e) confirms a complete transformation of the freshly exfoliated flake to the 1T'-MoS₂ phase. This experimentally established 1T' phase formation is further verified by image simulation, which shows perfect matching of the theoretical diffraction patterns with the experimental SAED images (Fig. 1b, c). For reference, Supplementary Fig. 1 displays experimental and simulated SAED patterns for other MoS₂ polymorphs.

The first-principles calculations of 1T'-MoS₂, carried out both for monolayer and bulk cases (see Methods for details), confirm the ferroelectric nature of this structural phase. The computed atomic structure is given in Supplementary Table 1 (see also Supplementary Fig. 3). The 1T'-MoS₂ phase features a distorted octahedral unit cell (see Fig. 1d and Supplementary Fig. 3) with an out-of-plane dipole moment. Specifically, the in-plane displacement of

certain Mo atoms results in a periodic sublattice of Mo trimers centered at S atoms (termed here as "polar") embedded into a S-Mo-S matrix with atoms located near their ideal positions in the undistorted octahedral structure²³. Due to the reduced distance between the trimerized Mo atoms, the polar S atoms (marked by the dashed blue circles in Fig. 1d) as well as those bridging the trimers (marked by the dashed red circles in Fig. 1d) are pushed up from their original positions to maintain their bond lengths to the shifted Mo atoms. This vertical displacement of the S atoms is tantamount to the occurrence of an out-of-plane polarization. A direct comparison of the atomic arrangement in the 1T' phase with the parent 1T phase is shown in Supplementary Fig. 4.

The electronic band structures computed for the monolayer and bulk 1T'-MoS₂ (Supplementary Fig. 5) provide a deeper insight into the electronic and polar behavior of the 1T' phase (see Methods for details). The monolayer-thick 1T'-MoS₂ exhibits a semiconductor state with a direct band gap of 0.19 eV at the *K* point of the Brillouin zone. On the other hand, for the bulk (multilayer) 1T'-MoS₂, we observe a significant dispersion along the stacking direction (Γ -Z line), in spite of the typically large interlayer separation of 5.96 Å in the relaxed bulk structure. As a result, the multilayer 1T'-MoS₂ is found to be metallic. The experimental evidence of the metallic behavior of 1T'-MoS₂ phase is provided in Supplementary Fig. 6. Nevertheless, a polarization estimate by computing the dipole moment of an isolated monolayer is still feasible and yields the value of 0.04 μC cm⁻² (Fig. 2a), which is smaller than that predicted for the d1T-MoS₂ polymorph² but definitely sizeable. Hence, according to our modeling, multilayer 1T'-MoS₂ can be considered as a polar metal³⁰.

Interestingly, the obtained sign for the polarization (Fig. 1d) is opposite to what one would expect from the polar ionic displacements: the polarization is aligned in the direction of the visible S anion shift, instead of being opposite to it. To gain further insight into this effect, in Fig. 2b we plot the charge density obtained for the 1T' phase, a centrosymmetric (*P3m1*) reference phase constructed by removing the polar distortion from the 1T' structure, and the difference charge density between the two. We find that the "polar" S atoms do create a dipole opposite to their movement, with a displaced negative charge (shown as cyan lobes in Fig. 2b) following their movement. However, we also observe that the remaining S atoms (which barely move along the vertical direction) have an oppositely-oriented electron redistribution associated with them, an effect likely driven by the in-plane displacement of the Mo atoms. The net polarization aligns with the latter contribution, indicating that the seemingly inert S atoms overcome the polarization created by the polar ones. This surprising result is reminiscent of previous observations of anomalous dynamical charges in the 1T-MoS₂ structures, which have been attributed to a strong covalency in these compounds and the proximity to metallic phases³¹.

The experimental testing of the polar state of 1T'-MoS₂ has been carried out by measuring the electromechanical response of the flakes by PFM. The flake thickness in these studies is in the range of 5–20 nm. Figure 3a–c show the topography of a representative as-prepared (pristine) 8-nm-thick 1T'-MoS₂ flake along with its corresponding PFM amplitude and phase images. Although the PFM amplitude exhibited by this particular sample is rather weak, a number of other pristine 1T'-MoS₂ flakes exhibit the PFM amplitude signal that is about 3–4 times above the noise level (see Supplementary Fig. 7) providing initial evidence of the robust electromechanical activity and a polar state of pristine 1T'-MoS₂. Yellow color in the PFM phase image (Fig. 3c) represents an "in-phase" electromechanical response to a sensing ac field (i.e., an increase in the sample thickness for a positive half of the applied ac bias cycle, and sample thickness decrease for negative half of the ac bias cycle) and corresponds to the downward polarization direction (toward the substrate).

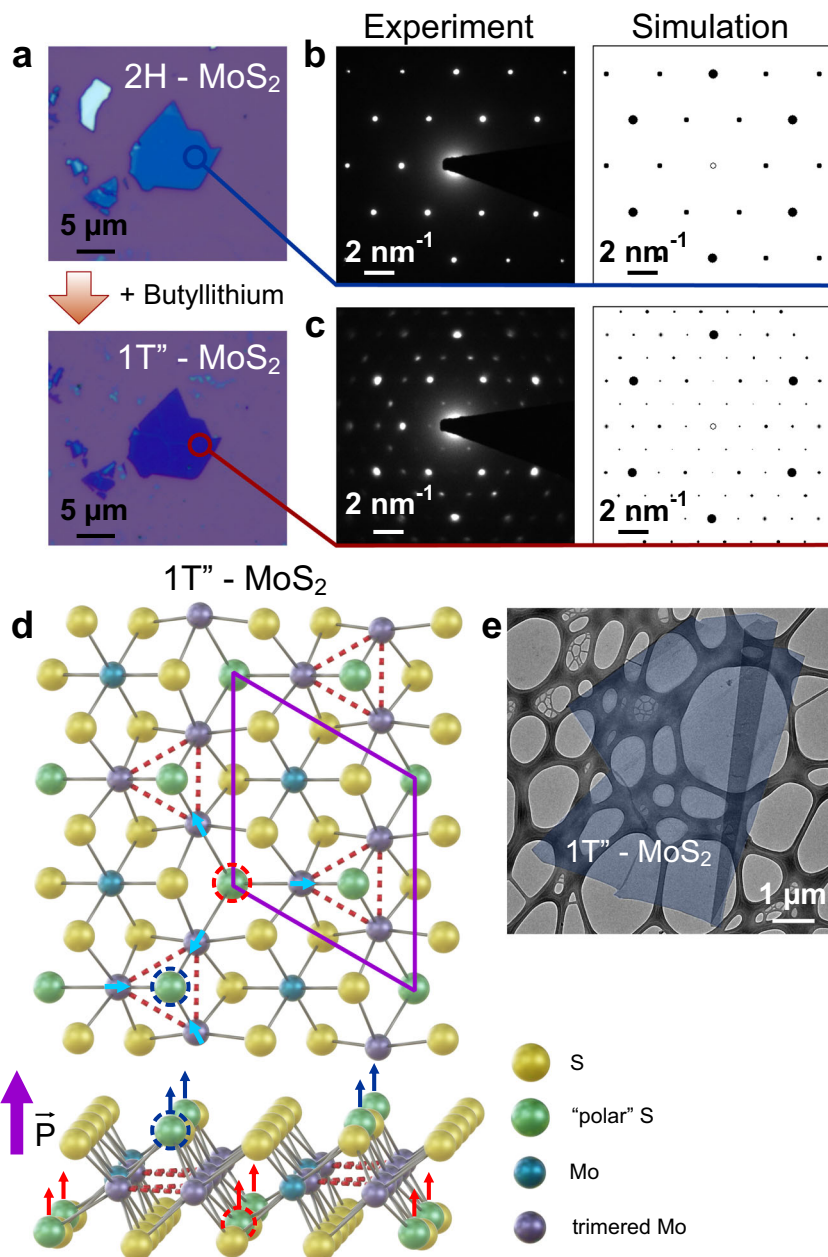


Fig. 1 Synthesis and structural characterization of 1T''-MoS₂ flakes. **a** MoS₂ flake on Si/SiO₂ substrate before and after the treatment with *tert*-butyllithium. **b, c** Experimental SAED patterns of the MoS₂ flakes before (**b**) and after (**c**) the lithiation treatment and the corresponding theoretical SAED patterns constructed using the calculated atomic positions in the unit cell with the trigonal symmetry (see Supplementary Table 1 and Supplementary Fig. 2). The SAED patterns in **b, c** correspond to 2H-MoS₂ and 1T''-MoS₂ phases, respectively. **d** Atomic structure of 1T''-MoS₂ (upper panel—top view, lower panel—side view). A unit cell is marked by the purple rhombus in the upper panel. Arrows in the upper panel illustrate the displacements of the Mo atoms forming trimers (marked by dashed triangles). The Mo and S atoms located close to the ideal positions in the undistorted 1T-MoS₂ structure are shown as blue and yellow spheres, respectively. Arrows in the lower panel illustrate the vertical displacements of the polar sulfur atoms in the centers of the trimers and sulfur atoms bridging the trimers (marked by the dashed blue and red circles, respectively) from their ideal positions. Vertical displacement of the S atoms results in the emergence of an out-of-plane polarization. **e** TEM image of a representative 1T''-MoS₂ flake (shown in blue for clarity) on a lacey carbon TEM grid.

A natural next step in establishing the ferroelectric properties of 1T''-MoS₂ would be the investigation of its polarization response under an applied electric field³². However, the high electrical conductance of 1T''-MoS₂ (note the metallic ground state of bulk 1T''-MoS₂ predicted by our DFT calculations) precludes the use of this standard approach. On the other hand, it has been previously demonstrated that strain gradients can play a role of an effective electric field due to the flexoelectric effect³³. Hence, highly

concentrated non-uniform stress produced by the PFM tip pressed against the sample surface (Fig. 3d) can be used as an efficient tool for polarization reversal in highly conductive MoS₂ samples, thereby eliminating the need for electric field application. The outcome of this approach is illustrated in Fig. 3e, f. Scanning a 5 × 5 μm² area with the PFM tip under an applied load of 1100 nN (well above the 100 nN load used during conventional PFM measurements) results in an enhanced PFM amplitude signal

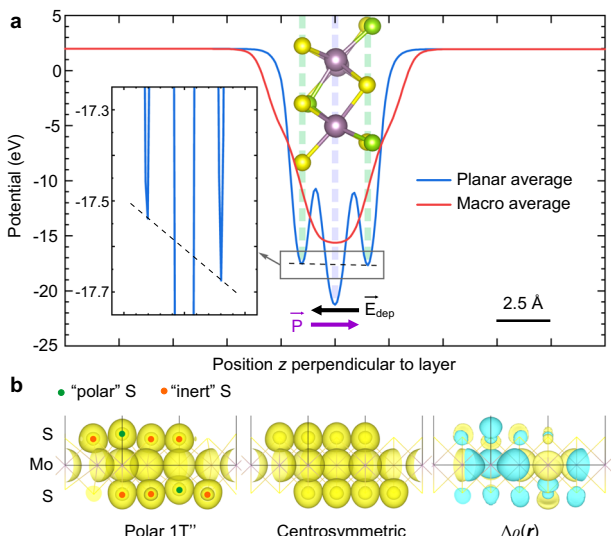


Fig. 2 First-principles simulations of internal potential and polarization for a 1T'-MoS₂ monolayer. **a** The calculated potential is a three-dimensional function. The “planar-average” potential is calculated as a function of z (i.e., in the direction perpendicular to the S-Mo-S layer) by averaging in z -planes. The three potential wells of the planar-average potential coincide with the planes containing the S and Mo atoms (see the atomic structure in inset with atoms colored as in Fig. 1d). The macroscopic-average potential, commonly used to identify the depolarizing fields, is calculated by averaging the planar-average potential over a 3 Å-wide trailing window. It is found that the depolarizing field here cannot be clearly observed in this way as the trailing window is comparable with the total width of the layer. Nevertheless, the planar-average potential does show that the potential well associated with the S atoms to the right of the Mo plane is slightly deeper than the well associated with the S atoms to the left (see zoom-in inset), which is indicative of a depolarizing field pointing to the left and, thus, an electric dipole pointing to the right. **b** Side view of the 1T'-MoS₂ monolayer, showing the computed electronic charge density for the polar state (left panel) and a reference centrosymmetric structure obtained by removing the polar distortion from the polar one (center panel). The final figure (right panel) shows a charge density difference, where cyan lobes indicate an excess of electrons in the polar state. In the left image, the charged density of “polar” and seemingly “inert” sulfur atoms are labeled by green and orange dots, respectively.

(Fig. 3e) and PFM phase reversed by 180° (Fig. 3f), which is a strong indication of the robust polarization switched by the tip-induced mechanical stress. Topographic imaging does not show any sample damage and only minor (about 0.5 nm) depression on the flake surface subjected to stress. The switched polarization state is highly stable as the PFM amplitude and phase signals monitored over a period of several weeks did not show any significant decay. It is worth mentioning that the observed effect is independent of the type of substrate material as it has been observed in the flakes on Pt, Au, and La_{0.67}Sr_{0.33}MnO₃ electrodes (see Supplementary Fig. 7). For reference, the same mechanical switching approach has been applied to the non-polar semiconducting allotrope of molybdenum disulfide with hexagonal symmetry, 2H-MoS₂ (See Supplementary Fig. 8). Notably, no change in the PFM response has been observed indicating that the induced switching seen in Fig. 3e, f is inherently related to the ferroelectric nature of 1T'-MoS₂.

Further characterization of 1T'-MoS₂ with respect to its ferroelectric behavior involved testing of the mechanically-switched state by a set of complementary local probe microscopy techniques. Results of application of Laser Doppler Vibrometer (LDV) spectroscopy, which enables quantitative measurements of

the piezoelectric response by direct measurements of the cantilever displacement in PFM experiments³⁴, are shown in Fig. 3g. It is seen that while the pristine area of the 1T'-MoS₂ flake exhibits a measurable piezoelectric coefficient d_{33} of 0.7 ± 0.4 pm/V (which is slightly above the noise level of 0.3 pm/V), the mechanically poled region is characterized by a much higher d_{33} value of 2.8 ± 0.4 pm/V. Nearly flat frequency response in the range from 50 to 275 kHz indicates a negligible contribution from the cantilever dynamics to the measured PFM amplitude signal suggesting unambiguous and accurate evaluation of the piezoelectric coefficient not affected by an instrumental background signal (Supplementary Fig. 9).

Kelvin probe force microscopy (KPFM) measurements (Fig. 3h) provide further evidence for the stress-induced switching of polarization in 1T'-MoS₂. It should be noted that in the case of perovskite ferroelectrics, such as BaTiO₃, the strain gradient due to the tip pressure switches polarization from the upward to the downward direction (see Supplementary Fig. 10)³⁵. However, 1T'-MoS₂ displays an opposite response: KPFM reveals a potential drop of 0.12 V in the region subjected to the tip-induced stress (as opposed to the potential increase in BaTiO₃ shown in Supplementary Fig. 10), which can be attributed to the negative screening charges compensating the bound charges of the upward polarization. Electrostatic force microscopy (EFM) imaging (Fig. 3i) of the same region also shows a contrast change consistent with the upward polarization corroborating the KPFM results. The KPFM/EFM data are in agreement with the PFM phase results (Fig. 3f). Overall, these findings indicate that the tip pressure switches 1T'-MoS₂ to the upward polarization state, i.e., opposite to that in perovskite ferroelectrics. This effect, which requires further investigation, might be related either to the anomalous behavior of polarization in 1T'-MoS₂, where the induced polarization is pointing in the same direction as the displacement of S anions rather than opposite to it, or to the negative value of the flexoelectric coefficient.

On the basis of the obtained structural data, computational modeling, and SPM characterization results, it is evident that pristine 1T'-MoS₂ exhibits a switchable polar state, i.e., 1T'-MoS₂ is ferroelectric. To explain a relatively weak PFM amplitude signal intermittently encountered in some pristine 1T'-MoS₂ samples, we performed additional testing experiments on the flakes that have been flipped over (Fig. 4a) (see also “Methods” and Supplementary Fig. 11 for details). It is natural to expect that after flipping a polarized pristine 1T'-MoS₂ flake would exhibit a different PFM phase contrast due to the reversed polarization direction, while its PFM amplitude signal would remain the same. However, the obtained results turned out to be more complicated than expected. Figure 4 shows two 1T'-MoS₂ flakes (#1 and #2) with the downward polarization in the pristine state (Fig. 4b) where the central regions were poled upward by the tip-induced mechanical stress (Fig. 4c). After flipping them over, flake #1 exhibited the inverted PFM phase contrast corresponding to the upward polarization, while flake #2 still displayed the phase contrast consistent with the downward polarization (Fig. 4d). Moreover, both flakes displayed a uniform phase contrast showing no traces of the mechanically poled regions. After the flakes had been flipped back, the previously poled regions were still present manifesting their remarkable stability against the changing chemical and mechanical boundary conditions (Fig. 4e). The PFM amplitude images complementary to the data in Fig. 4b–e are shown in Supplementary Fig. 12.

These results can be understood if one assumes that oppositely polarized layers can coexist within a 1T'-MoS₂ flake, thus forming head-to-head (H-H) and tail-to-tail (T-T) dipole configurations (Fig. 4f), which we term as “antipolar.” From this point of view, the fact that, upon flipping, flake #2 exhibits unchanged PFM phase contrast with respect to the pristine state indicates that both the top and bottom layers in this flake exhibit inward polarization

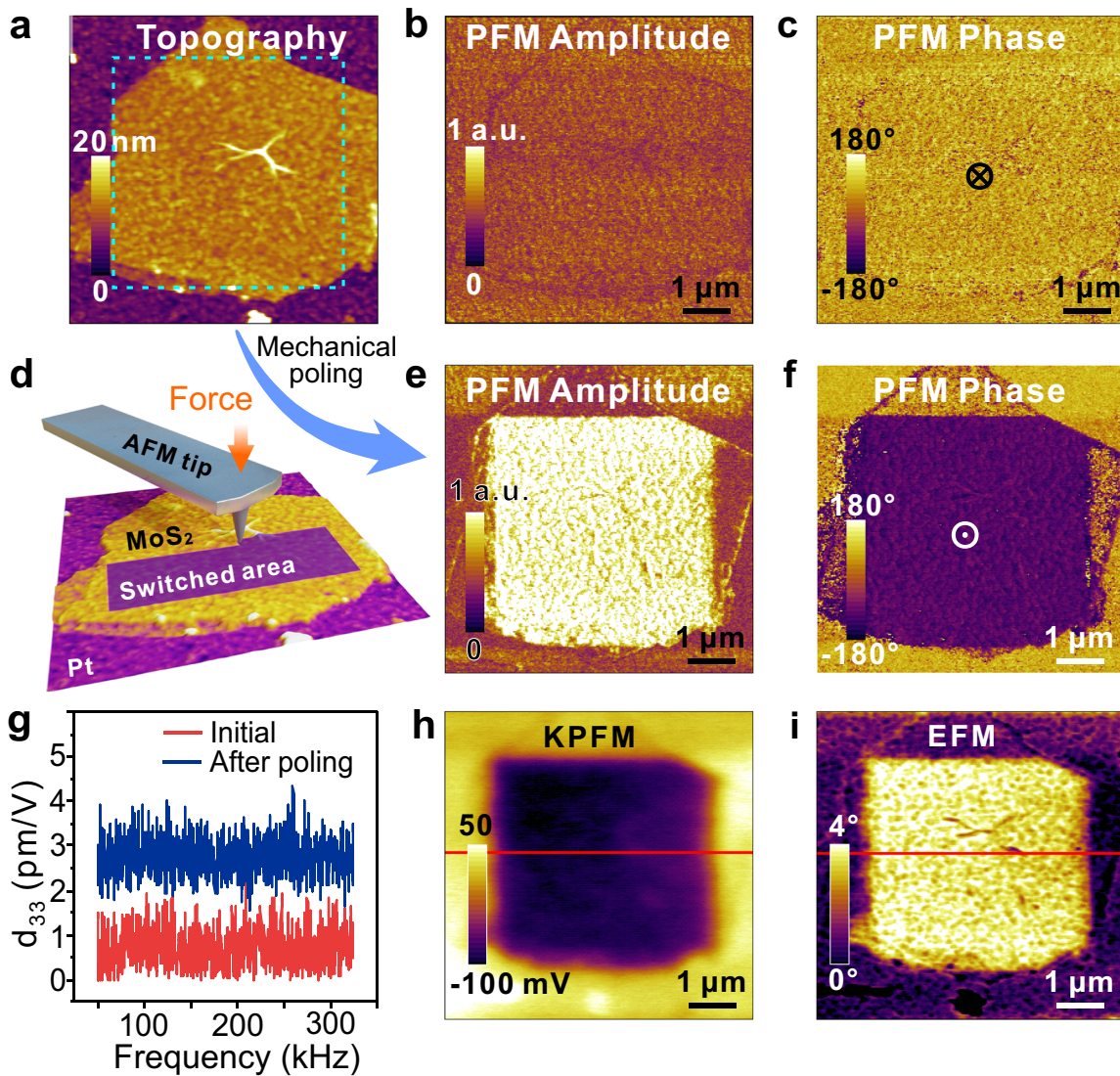


Fig. 3 Probing the electromechanical and electrical properties of 1T''-MoS₂. **a** Topographic image of the pristine 8-nm-thick flake. The dashed line represents the $5 \times 5 \mu\text{m}^2$ region that is subjected to a mechanical load of 1100 nN. **b, c** PFM amplitude (**b**) and phase (**c**) images of the pristine 1T''-MoS₂ flake. **d** Schematics of an experiment on application of mechanical stress by a PFM tip. **e, f** PFM amplitude (**e**) and phase (**f**) images of the same 1T''-MoS₂ flake after application of mechanical stress. **g** The frequency-dependent piezoelectric response acquired by LDV in the pristine and mechanically poled regions of the 1T''-MoS₂ flake. **h, i** KPFM (**h**) and EFM (**i**) maps of the 1T''-MoS₂ flake after application of mechanical stress. A bright region in the EFM phase image (**i**) acquired with a dc read bias of +3 V corresponds to the negative surface charge, which is further corroborated by the reduced contact potential difference in the same region seen in the KPFM image (**h**).

(Fig. 4h), while in flake #1 these layers are aligned in the same direction (Fig. 4g). A stress gradient applied to the flake with the downward polarization is expected to induce switching to the upward state, but only in the topmost layers and not across the whole thickness of the flake, as the strain is concentrated in a small volume right underneath the pressing tip^{35,36}. It has been found that even flakes as thin as 5 nm could not be switched completely across their thickness, which explains the non-appearance of the poled regions in the thicker flipped flakes in Fig. 4d. Thicker flakes might have irregular combinations of the oppositely poled layers with H-H and T-T dipole configurations, which would explain variability of the PFM amplitude signals in the pristine and poled 1T''-MoS₂ flakes.

The existence of stable antipolar dipole configurations is also confirmed by the second harmonic generation (SHG) measurements³⁷ (see “Methods” and Supplementary Fig. 13), which reveal a significant difference between the signals from the pristine and

mechanically poled regions in 1T''-MoS₂. Observation of a robust nonlinear optical response from the pristine 1T''-MoS₂ (see Supplementary Fig. 14) is indicative of its polar nature. It should be noted that the oppositely polarized layers are characterized by the same SHG susceptibility tensor components but with opposite signs. On the other hand, because of the quadratic dependence of the SHG intensity on the susceptibility, mutually antiparallel domains are expected to exhibit the same SHG intensity but with a phase shift of π (see Supplementary Information for details). Thus, the reduced intensity observed in the mechanically poled area with respect to the surrounding region (Supplementary Fig. 14) is consistent with an incomplete reversal of the polarization across the flake thickness: its lower SHG contrast is due to the destructive interference between the two π -shifted signals (Supplementary Fig. 13).

A coexistence of highly stable oppositely polarized layers in 1T''-MoS₂ requires additional consideration. The H-H and T-T interfaces

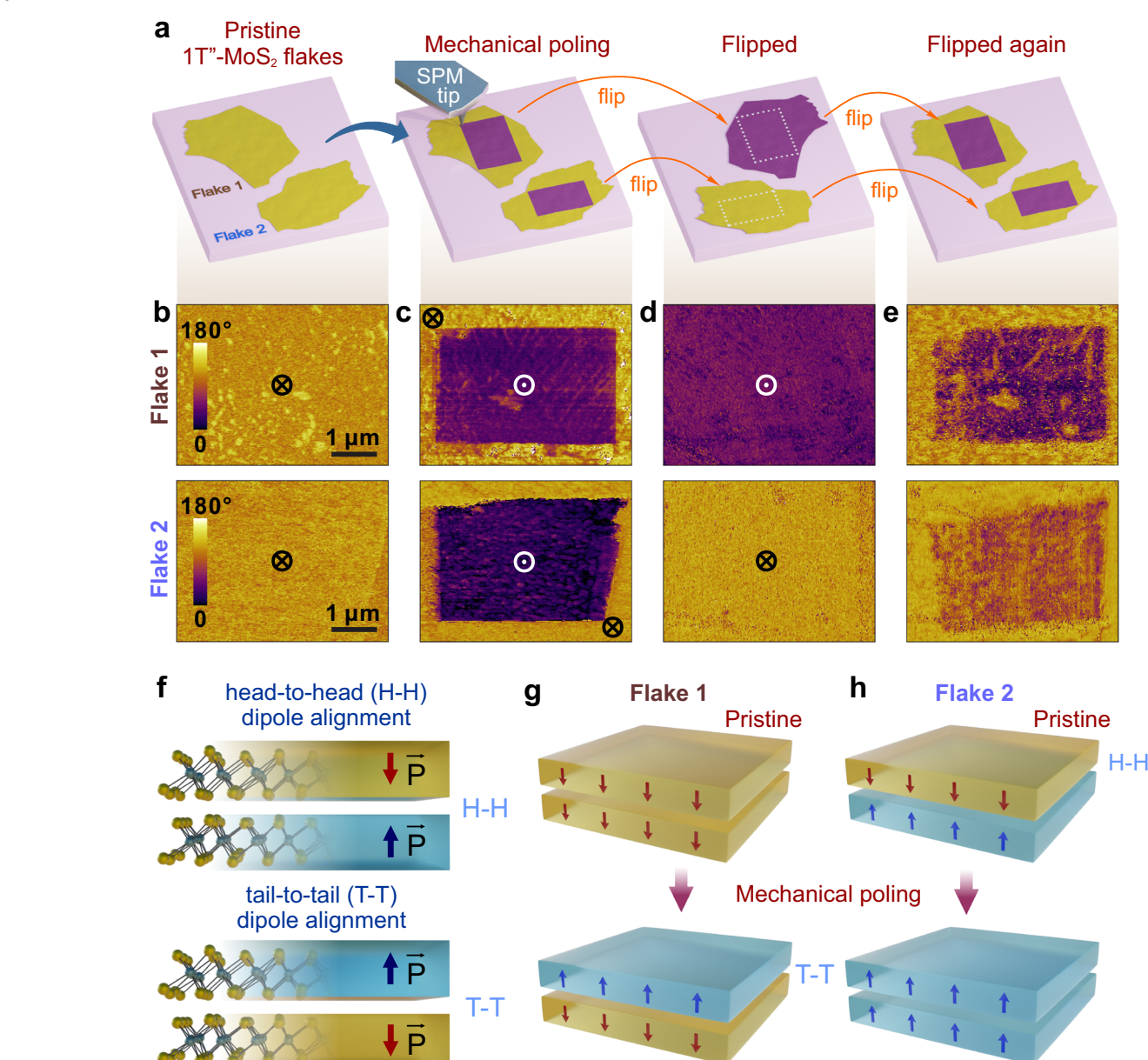


Fig. 4 Observation of the PFM signals in the flipped 1T''-MoS₂ flakes. **a** Scheme of the experiment that involves mechanical poling and flipping of the flakes. **b** PFM phase images of two pristine 8-nm-thick 1T''-MoS₂ flakes with downward polarization. **c** PFM phase images of the same flakes after application of a mechanical load of 1100 nN to their central regions resulting in the switching to the upward polarization state. **d** PFM phase images of the same flakes after they were flipped over and placed on the same substrate. The entire flake #1 exhibits the upward polarization, while the entire flake #2 exhibits the downward polarization. **e** PFM phase images of the same flakes after they were flipped back to their original orientation. **f** Illustrations of the antipolar H-H and T-T dipole alignments. **g, h** Schemes of the dipole alignments in flakes #1 and #2 in their pristine state and after mechanical poling corresponding to the experimental results shown in **b–e**.

should be charged due to the polarization discontinuity, i.e., $\nabla \cdot P \neq 0$. In conventional perovskite ferroelectric materials, such as PbTiO₃ or BaTiO₃, such charged domain walls are hard to obtain; however, they are frequently observed in ferroelectrics with a small value of spontaneous polarization and efficient electronic screening (for example, hexagonal manganites³⁸). Since 1T''-MoS₂ displays a weak polarization and metallic conductivity along the stacking direction, it clearly belongs to the latter category. To verify the feasibility of the stable H-H and T-T dipole alignments, we performed first-principles calculations of the antipolar 1T''-MoS₂ with the results summarized in Supplementary Fig. 15. It has been found that in the antipolar state, the individual MoS₂

monolayers retain their polarization. The calculated antipolar interface energy (an average of the H-H and T-T cases, as they appear in pairs in the periodically-repeated simulation supercell) is 18 mJ m⁻², which is very small compared to a typical value of the domain-wall energy in classic ferroelectric materials (for example, the energies of neutral domain walls commonly observed in PbTiO₃ range between 30 and 130 mJ m⁻²³⁹). This result confirms that the antipolar H-H and T-T dipole alignments in 1T''-MoS₂ are thermodynamically stable.

In summary, using a combination of the synthesis, first-principles modeling, structural characterization, and SPM probing of the electromechanical properties, we have demonstrated the

ferroelectric behavior of 2D 1T'-MoS₂—a polar metal with switchable polarization. We have found unambiguous evidence of a stable antipolar structure consisting of oppositely polarized layers where polarization can be switched by tip-induced mechanical pressure due to the flexoelectric effect. The head-to-head and tail-to-tail dipole arrangements give rise to wide variability of piezoresponse and associated electronic properties of 1T'-MoS₂ due to the formation of the charged interfaces between adjacent polar layers. The coexistence of switchable polarization and metallic conduction makes 1T'-MoS₂ a member of a handful of materials with this unique property. Overall, the experimental demonstration of ferroelectricity in 2D molybdenum disulfide opens new perspectives for the fundamental studies of this compound and enables new functionality, which could be exploited in novel electronic applications.

METHODS

Fabrication of 1T'-MoS₂ samples

All chemicals were purchased from Sigma-Aldrich and used as received unless noted otherwise. 2H-MoS₂ flakes with thicknesses ranging from 5 nm to 20 nm were exfoliated from commercial MoS₂ crystals (SPI supplies) using an adhesive tape and deposited on conductive (Pt/SiO₂/Si) substrates. The samples were transferred to a nitrogen-filled glovebox, where they were soaked in dry hexane for 5 min and then in 2.5 M solution of *tert*-butyllithium in hexane for 3 h. The produced 1T'-MoS₂ flakes were then soaked in dry hexane and rinsed with ethanol to remove possible lithium residues²⁴. Optical microscopy was conducted to locate flakes with uniform colors and clean surfaces, which were used for further studies.

Structural characterization of the MoS₂ samples

Raman spectra of the pristine and lithiated MoS₂ flakes were recorded using a Thermo Scientific DXR Raman microscope with a 532 nm excitation laser. A relatively low laser power of 2 mW was used to prevent possible phase transformations in MoS₂ flakes due to overheating. TEM images and SAED diffraction patterns of MoS₂ flakes were recorded using a FEI Tecnai Osiris scanning transmission electron microscope equipped with a HAADF detector and a X-FEG high brightness Schottky field emission gun; the accelerating voltage was 200 kV. The flakes were transferred from Pt/SiO₂/Si substrates to a TEM grid using a sacrificial cellulose film. Analysis of the diffraction patterns was performed with the CrysTBox software⁴⁰ using MoS₂ structural models from ref.²³.

Flipping procedure of 1T'-MoS₂ flakes

First, (i) MoS₂ flake on Pt substrate is covered by cellulose solution in ethyl acetate and let dry in air for 5 min (Supplementary Fig. 11). (ii) The cellulose forms a semitransparent film, making it easy to locate the flake and confirm it was not detached from the substrate. The sides of the substrate should be cleaned from the cellulose film by a razor blade to prevent its sticking in the next step. (iii) Then one of the substrate's side is partially submerged under DI water so that the surface of the water slightly covers the cellulose film. When water permeates the interface between the substrate and the film, the latter detaches from the substrate and floats on the surface of the water. The substrate is slowly submerged further until the entire substrate is underwater, and the film is floating freely. Since adhesion between cellulose and a flake is stronger than that between the flake and a substrate, the cellulose film carries the MoS₂ flake with it on water. The advantage of using cellulose is that the transfer can be made from various substrates, including conductive Pt, and does not require using toxic chemicals like HF. (iv) The floating film is then fished out by a thick (~2 mm) and firm polydimethylsiloxane (PDMS) film. (v) After drying for 5 min in the air, the PDMS is cleaned with ethyl acetate, which is gently poured on the substrate for 2 min to dissolve the cellulose. After drying, (vi) clean MoS₂/PDMS film is flipped over, placed on a new Pt-covered substrate with MoS₂ facing down, and gently pressed to ensure adhesion between the flake and the substrate. Finally, (vii) the PDMS film is carefully peeled off, revealing the flipped MoS₂ flake resting on a Pt-covered substrate.

A. Lipatov et al.

Local probe microscopy measurements

Local SPM measurements were performed using a commercial atomic force microscopy (AFM) system (MFP-3D, Asylum Research) with Pt-coated conductive AFM tips (PPP-EFM, Nanosensors). For PFM imaging, an ac modulation bias with an amplitude of 0.5–0.8 V and frequency of 330–360 kHz was applied to the tip, which scanned the sample surface under a normal loading force <100 nN. Mechanical poling was realized by scanning a sample area in the contact mode under a high loading force (in the range from 300 nN up to 2000 nN) while both the tip and the bottom electrode were grounded. The cantilever spring constant was calibrated by the thermal noise method built-in in the AFM system.

KPFM imaging was performed in the two-pass regime: the first pass allowed mapping the topography, and the second pass enabled surface potential mapping with the tip kept at a constant height of 30 nm from the surface. During EFM imaging, which was also carried in the non-contact regime, a constant dc bias of +3 V was applied to the tip while the tip was oscillated at a frequency slightly below resonance around 75 kHz.

CAFM imaging and *I*-*V* spectroscopy were performed in the contact mode with a bias applied to the bottom electrode and current being collected via a current amplifier on a tip side. A read dc bias of 0.2 V was applied during CAFM imaging.

The interferometric LDV spectroscopy measurements were performed on a commercially available AFM system (Cypher S, Asylum Research) equipped with an interferometric displacement sensor option. For quantitative piezoelectric testing, the vertical displacement of the cantilever immediately above the tip location in response to the modulated tip-sample bias was directly measured via the interferometer system with the sub-picometer precision. The interferometer signal was collected at a fixed ac bias with 1 V amplitude for a frequency range from 20 to 800 kHz.

SHG measurements

The SHG measurements were conducted by means of a scanning confocal microscope in reflection geometry (Supplementary Fig. 13). The fundamental wave was provided by a Spectra Physics Ti:Al₂O₃ laser (Millenium-Tsunami combination), which generated 100 fs pulses with a repetition rate of 80 MHz and a wavelength centered at 800 nm. The laser beam was directed at normal incidence to the sample and focused with a $\times 60$ magnification objective lens (numerical aperture N.A. = 0.85). The SHG images were obtained by scanning the sample with respect to the incoming beam using computer-controlled stepping motors with a minimum step of 50 nm and recording the SHG signal at each scan step with a typical exposure time of 100 ms/step at a power of 30 mW. The output intensity was spectrally filtered and collected into a photomultiplier. Motorized polarizer and analyzer allowed for polarimetry analysis.

First-principles simulations

A density functional theory (DFT) as implemented in the software package VASP^{41,42} has been used for first-principles modeling. We have verified that the so-called “PBEsol” energy functional⁴³ yields the structural parameters (particularly, the out-of-plane lattice constant) comparable to experimental values for the 1T-MoS₂ phase. Specifically, PBEsol renders 6.12 Å, which is in good agreement with the experimental data ranging from 6.15 to 6.29 Å⁴⁴. In contrast, a “PBE” functional⁴⁵ yields a too-long interlayer spacing (7.04 Å), and the various van der Walls corrections render scattered results that do not improve over the PBEsol solution. Hence, given that in the polar phases of interest, the unscreened short-range electrostatic interactions controlling the coupling between layers can be expected, we used the regular PBEsol approximation. The interaction between the core and valence electrons was treated within the Projector-Augmented Wave approach⁴⁶, solving explicitly for the following electrons: Mo's 4s, 4p, 4d and 5s, and S's 3s and 3p. Reciprocal space integrals were computed using an $8 \times 8 \times 8$ k-point grid for a typical bulk-like supercell with 4 formula units, and equivalent grids when bigger supercells were employed. We explicitly checked that the calculation conditions were well-converged for our current purposes (e.g., energy differences between the 1T' and d1T polymorphs of MoS₂ were converged to within 1 meV per Mo atom for a $6 \times 6 \times 6$ k-point grid).

For the calculations of multilayer (bulk) 1T'-MoS₂, in both the monodomain and polydomain states, we considered different stacking of the layers (up to four possibilities per case), running relaxations where no symmetry was imposed. All relaxations converged to the structures here reported, which can thus be taken as robust energy minima.

DATA AVAILABILITY

All relevant data that support the findings of this study are available in the article and its supplementary files. Source data for Figs. 2a and 3g and other additional data are available from the authors upon request.

CODE AVAILABILITY

The simulations were run using the Vienna Ab Initio Simulation Package (VASP), a proprietary code that can be obtained from the developers (see www.vasp.at). For the analysis, we used the VASPKIT package (<http://vaspkit.com/>) and we used the VESTA code to prepare some figures (<https://jp-minerals.org/vesta/en/>); both of them can be freely obtained from the indicated sites. The diffraction patterns were simulated using the CrysTBox, which is available from the developer (see www.fzu.cz/crystbox).

Received: 7 December 2021; Accepted: 9 February 2022;

Published online: 15 March 2022

REFERENCES

- Wu, W. et al. Piezoelectricity of single-atomic-layer MoS₂ for energy conversion and piezotronics. *Nature* **514**, 470–474 (2014).
- Shirodkar, S. N. & Waghmare, U. V. Emergence of ferroelectricity at a metal-semiconductor transition in a 1T monolayer of MoS₂. *Phys. Rev. Lett.* **112**, 157601 (2014).
- Fei, Z. et al. Ferroelectric switching of a two-dimensional metal. *Nature* **560**, 336–339 (2018).
- Ding, W. et al. Prediction of intrinsic two-dimensional ferroelectrics in In₂Se₃ and other III₂-VI₃ van der Waals materials. *Nat. Commun.* **8**, 14956 (2017).
- Yang, Q., Xiong, W., Zhu, L., Gao, G. & Wu, M. Chemically functionalized phosphorene: two-dimensional multiferroics with vertical polarization and mobile magnetism. *J. Am. Chem. Soc.* **139**, 11506–11512 (2017).
- Wu, M., Burton, J. D., Tsymbal, E. Y., Zeng, X. C. & Jena, P. Hydroxyl-decorated graphene systems as candidates for organic metal-free ferroelectrics, multiferroics, and high-performance proton battery cathode materials. *Phys. Rev. B* **87**, 081406(R) (2013).
- Cui, C., Xue, F., Hu, W.-J. & Li, L.-J. Two-dimensional materials with piezoelectric and ferroelectric functionalities. *NPJ 2D Mater. Appl.* **2**, 18 (2018).
- Zhou, Y. et al. Out-of-plane piezoelectricity and ferroelectricity in layered α-In₂Se₃ nanoflakes. *Nano Lett.* **17**, 5508–5513 (2017).
- Zheng, C. et al. Room temperature in-plane ferroelectricity in van der Waals In₂Se₃. *Sci. Adv.* **4**, eaar7720 (2018).
- Chang, K. et al. Discovery of robust in-plane ferroelectricity in atomic-thick SnTe. *Science* **353**, 274–278 (2016).
- Higashitamura, N. et al. Purely in-plane ferroelectricity in monolayer SnS at room temperature. *Nat. Commun.* **11**, 2428 (2020).
- Sharma, P. et al. A room-temperature ferroelectric semimetal. *Sci. Adv.* **5**, eaax5080 (2019).
- Liu, F. et al. Room-temperature ferroelectricity in CulnP₂S₆ ultrathin flakes. *Nat. Commun.* **7**, 12357 (2016).
- You, L. et al. In-plane ferroelectricity in thin flakes of van der Waals hybrid perovskite. *Adv. Mater.* **30**, 1803249 (2018).
- Cheng, R. et al. Few-layer molybdenum disulfide transistors and circuits for high-speed flexible electronics. *Nat. Commun.* **5**, 5143 (2014).
- Lee, G.-H. et al. Flexible and transparent MoS₂ field-effect transistors on hexagonal boron nitride-graphene heterostructures. *ACS Nano* **7**, 7931–7936 (2013).
- Feng, J. et al. Identification of single nucleotides in MoS₂ nanopores. *Nat. Nanotechnol.* **10**, 1070–1076 (2015).
- Manzeli, S., Ovchinnikov, D., Pasquier, D., Yazyev, O. V. & Kis, A. 2D transition metal dichalcogenides. *Nat. Rev. Mater.* **2**, 17033 (2017).
- Mak, K. F., Lee, C., Hone, J., Shan, J. & Heinz, T. F. Atomically thin MoS₂: a new direct-gap semiconductor. *Phys. Rev. Lett.* **105**, 136805 (2010).
- Radisavljevic, B., Radenovic, A., Brivio, J., Giacometti, V. & Kis, A. Single-layer MoS₂ transistors. *Nat. Nanotechnol.* **6**, 147–150 (2011).
- Kappera, R. et al. Phase-engineered low-resistance contacts for ultrathin MoS₂ transistors. *Nat. Mater.* **13**, 1128 (2014).
- Yu, Y. et al. High phase-purity 1T'-MoS₂- and 1T'-MoSe₂-layered crystals. *Nat. Chem.* **10**, 638–643 (2018).
- Chou, S. S. et al. Understanding catalysis in a multiphasic two-dimensional transition metal dichalcogenide. *Nat. Commun.* **6**, 8311 (2015).
- Guo, Y. et al. Probing the dynamics of the metallic-to-semiconducting structural phase transformation in MoS₂ crystals. *Nano Lett.* **15**, 5081–5088 (2015).
- Sharma, C. H., Surendran, A. P., Varghese, A. & Thalakulam, M. Stable and scalable 1T MoS₂ with low temperature-coefficient of resistance. *Sci. Rep.* **8**, 12463 (2018).
- Liu, L. et al. Phase-selective synthesis of 1T' MoS₂ monolayers and heterophase bilayers. *Nat. Mater.* **17**, 1108–1114 (2018).
- Guo, C. et al. Observation of superconductivity in 1T'-MoS₂ nanosheets. *J. Mater. Chem. C* **5**, 10855–10860 (2017).
- Yang, D., Sandoval, S. J., Divagalpitiya, W. M. R., Irwin, J. C. & Frindt, R. F. Structure of single-molecular-layer MoS₂. *Phys. Rev. B* **43**, 12053–12056 (1991).
- Chrissafis, K. et al. Structural studies of MoS₂ intercalated by lithium. *Mater. Sci. Eng. B* **3**, 145–151 (1989).
- Zhao, H. J. et al. Meta-screening and permanence of polar distortion in metallized ferroelectrics. *Phys. Rev. B* **97**, 054107 (2018).
- Choi, J.-H. & Jhi, S.-H. Origin of robust out-of-plane ferroelectricity in d1T-MoS₂ monolayer. *J. Phys. Condens. Matter* **32**, 045702 (2020).
- Gruverman, A., Alexe, M. & Meier, D. Piezoresponce force microscopy and nanoferroic phenomena. *Nat. Commun.* **10**, 1661 (2019).
- Lu, H. et al. Mechanical writing of ferroelectric polarization. *Science* **336**, 59–61 (2012).
- Labuda, A. & Proksch, R. Quantitative measurements of electromechanical response with a combined optical beam and interferometric atomic force microscope. *Appl. Phys. Lett.* **106**, 253103 (2015).
- Očenášek, J. et al. Nanomechanics of flexoelectric switching. *Phys. Rev. B* **92**, 035417 (2015).
- Lu, H. et al. Nanodomain engineering in ferroelectric capacitors with graphene electrodes. *Nano Lett.* **16**, 6460–6466 (2016).
- Xiao, J. et al. Intrinsic two-dimensional ferroelectricity with dipole locking. *Phys. Rev. Lett.* **120**, 227601 (2018).
- Meier, Q. N. et al. Global formation of topological defects in the multiferroic hexagonal manganites. *Phys. Rev. X* **7**, 041014 (2017).
- Íñiguez, J. First-Principles Studies of Structural Domain Walls. in Domain Walls: From Fundamental Properties to Nanotechnology Concepts (eds D. Meier, J. Seidel, M. Gregg, & R. Ramesh) (Oxford University Press, 2020).
- Klinger, M. More features, more tools, more CrysTBox. *J. Appl. Crystallogr.* **50**, 1226–1234 (2017).
- Kresse, G. & Furthmüller, J. Efficient iterative schemes for ab initio total-energy calculations using a plane-wave basis set. *Phys. Rev. B* **54**, 11169–11186 (1996).
- Kresse, G. & Joubert, D. From ultrasoft pseudopotentials to the projector augmented-wave method. *Phys. Rev. B* **59**, 1758–1775 (1999).
- Perdew, J. P. et al. Restoring the density-gradient expansion for exchange in solids and surfaces. *Phys. Rev. Lett.* **100**, 136406 (2008).
- Samadi, M. et al. Group 6 transition metal dichalcogenide nanomaterials: synthesis, applications and future perspectives. *Nanoscale Horiz.* **3**, 90–204 (2018).
- Perdew, J. P., Burke, K. & Ernzerhof, M. Generalized gradient approximation made simple. *Phys. Rev. Lett.* **77**, 3865–3868 (1996).
- Blochl, P. E. Projector augmented-wave method. *Phys. Rev. B Condens. Matter* **50**, 17953–17979 (1994).

ACKNOWLEDGEMENTS

This work was supported through the Nebraska Materials Research Science and Engineering Center (MRSEC, grant DMR-1420645) (to A.L., H.L., D.-F.S., E.Y.T., A.S., and A.G.) and by the National Science Foundation (NSF) grant DMR-1709237 (P.C. and A.G.). Z.G. acknowledges support from China Scholarship Council. This research was performed in part in the Nebraska Nanoscale Facility: National Nanotechnology Coordinated Infrastructure, which was supported by the NSF (ECCS-1542182) and the Nebraska Research Initiative. J.I. acknowledges the support of the Luxembourg National Research Fund through Grants INTER/MOBILITY/16/11467860 “2D-Ferro” and FNR/C18/MS/12705883 “REFOX”. S.C.-H. acknowledges funding from the French National Research Agency (contract ANR-18-CE92-0052-01).

AUTHOR CONTRIBUTIONS

A.G. conceived the idea and coordinated this work. A.S. supervised the sample preparation and structural characterization. A.L. and G.L. prepared the samples. A.L. performed structural characterization. P.C., Z.G., and H.L. performed scanning probe microscopy measurements; O.C., K.D.D., and S.C.-H. carried out second harmonic generation measurements. Laser Doppler Vibrometer measurements were performed by H.L. and R.P. J.I. carried out theoretical modeling. D.-F.S. and E.Y.T. contributed to theoretical discussions and commented on the manuscript. A.L., S.C.-H., J.I., A.S., and A.G. co-wrote the manuscript. All authors have given approval to the final version of the manuscript.

COMPETING INTERESTS

The authors declare no competing interests.

ADDITIONAL INFORMATION

Supplementary information The online version contains supplementary material available at <https://doi.org/10.1038/s41699-022-00298-5>.

Correspondence and requests for materials should be addressed to Jorge. Íñiguez, Alexander Sinitskii or Alexei Gruverman.

Reprints and permission information is available at <http://www.nature.com/reprints>

Publisher's note Springer Nature remains neutral with regard to jurisdictional claims in published maps and institutional affiliations.



Open Access This article is licensed under a Creative Commons Attribution 4.0 International License, which permits use, sharing, adaptation, distribution and reproduction in any medium or format, as long as you give appropriate credit to the original author(s) and the source, provide a link to the Creative Commons license, and indicate if changes were made. The images or other third party material in this article are included in the article's Creative Commons license, unless indicated otherwise in a credit line to the material. If material is not included in the article's Creative Commons license and your intended use is not permitted by statutory regulation or exceeds the permitted use, you will need to obtain permission directly from the copyright holder. To view a copy of this license, visit <http://creativecommons.org/licenses/by/4.0/>.

© The Author(s) 2022